

The effect of static pressure on the inertial cavitation threshold

Kenneth B. Bader,^{a)} Jason L. Raymond, Joel Mobley, and Charles C. Church

Department of Physics, University of Mississippi, National Center for Physical Acoustics, 1 Coliseum Drive, University, Mississippi 38677

D. Felipe Gaitan

Impulse Devices, Inc., 13366H Grass Valley Avenue, Grass Valley, California 95945-9549

(Received 7 March 2012; revised 12 June 2012; accepted 15 June 2012)

The amplitude of the acoustic pressure required to nucleate a gas or vapor bubble in a fluid, and to have that bubble undergo an inertial collapse, is termed the inertial cavitation threshold. The magnitude of the inertial cavitation threshold is typically limited by mechanisms other than homogeneous nucleation such that the theoretical maximum is never achieved. However, the onset of inertial cavitation can be suppressed by increasing the static pressure of the fluid. The inertial cavitation threshold was measured in ultrapure water at static pressures up to 30 MPa (300 bars) by exciting a radially symmetric standing wave field in a spherical resonator driven at a resonant frequency of 25.5 kHz. The threshold was found to increase linearly with the static pressure; an exponentially decaying temperature dependence was also found. The nature and properties of the nucleating mechanisms were investigated by comparing the measured thresholds to an independent analysis of the particulate content and available models for nucleation.

© 2012 Acoustical Society of America. [http://dx.doi.org/10.1121/1.4733539]

PACS number(s): 43.35.Ei, 43.25.Gf [NAG]

Pages: 728–737

I. INTRODUCTION

The energy concentration responsible for sonoluminescence (SL) has been known for some years,¹ and the large pressures and temperatures reached within the bubble have led some to speculate on whether thermonuclear conditions are attainable.² The recent work by Gaitan *et al.*³ concerns mechanisms for driving the collapse of bubbles. By increasing the static pressure of the fluid, they found that the amplitude of emitted shock waves and SL flashes from transient cavitation events increased 1000-fold over those measured for single bubble SL.^{3,4} These observations suggest that elevated static pressures have the potential to facilitate the creation of the conditions necessary for thermonuclear fusion.

The transient events observed by Gaitan *et al.*³ occur after a threshold tension has been achieved in the liquid. The cavitation threshold for water is well documented under various conditions,^{5–11} however, there are few data on the influence of static pressure above 10 MPa on the measurement. Pre-pressurization of the fluid samples has been shown to increase the threshold,^{12,13} which led Harvey to formulate the crevice model for nucleation.¹⁴ Greenspan and Tscheigg⁶ and Herbert *et al.*⁷ found that the absolute tension required for inertial cavitation was constant up to 80 bars static pressure. Strasberg⁹ also found that the required tension for inertial cavitation was constant when the static pressure was increased up to 4 bars, but noticed hysteresis in the measurement upon depressurization. These observations were consistent with the crevice model of Harvey *et al.*¹²

In this paper, the dependence of the inertial threshold on static pressure up to 300 bars (30 MPa) is reported. The

experimental setup and data collection procedure will be discussed first, followed by the experimental results. These results will then be compared to the crevice model for bubble nucleation as formulated by Crum.⁵

II. METHODS

A. Experimental setup

1. Acoustic resonator

The resonator is described in some detail by Gaitan *et al.*³ Briefly, the acoustic resonator [manufactured by Impulse Devices, Inc. (IDI), Grass Valley, CA] was a stainless steel (17-4), spherical shell with dimensions of 9.5 in. outer diameter and 8 in. inner diameter (3/4 in. thickness), and an approximate volume of 4.4ℓ . The resonator was machined as two separate hemispheres, which were joined by electron beam welding. Four ports provide access to the resonator's interior. Two of these ports were fitted with custom-made needle-type valves [1/2 in. National Pipe Thread (NPT) threads] allowing for circulation of fluid through the sphere. One of the remaining ports (1/4 in. NPT threads) was fit with a custom flush-mounted pressure sensor (603B1, Kistler Instrument Corporation, Amherst, NY). The remaining port (also 1/4 in. NPT) was sealed with a custom-made plug. The resonator was excited with four custom-designed transducers driven in parallel and mounted symmetrically about the resonator.

Measurements were made at zero-order, radially symmetric modes that are non-degenerate and are insensitive to geometrical imperfections to first order.¹⁵ Furthermore, the damping of the zero-order modes is only due to the properties of the fluid.¹⁵ This minimizes losses at resonance, resulting in large quality factors. It was empirically determined that modes near the intrinsic resonance of the drivers (~ 20 kHz)

^{a)}Author to whom correspondence should be addressed. Electronic mail: kenneth.bader@uc.edu

were most efficient at generating cavitation.³ For this reason, the (0,6) mode [$f \sim 25.5$ kHz, quality factor (Q) $\sim 10^4$] was chosen for the threshold measurements.

The radial pressure profile for these zero-order eigenmodes can be described by the spherical Bessel functions j_n ,

$$P(r) = P_0 j_n(k_{ns} r), \quad (1)$$

where k_{ns} is the wavenumber calculated from s th eigenfrequency of an n th order mode, and r is the radial distance from the center of the sphere. The measured radial pressure profiles were in agreement with Eq. (1) at driving amplitudes much lower than those used to initiate cavitation.¹⁶ Furthermore, the maximum pressure anti-node at $r=0$ was found to be linear with the driving amplitude near the cavitation threshold, as described in Ref. 17. These findings allowed the acoustic pressure to be measured at the inner radius of the resonator (~ 10.1 cm radius) with the pressure sensor and extrapolated to $r=0$ using Eq. (1), thus negating the need for an invasive probe.

2. Fluid loop

The resonator was incorporated into a closed-loop system, as shown in Fig. 1. The bulk of the loop was composed of stainless steel (types 303, 316, and 17-4), polytetrafluoroethylene (PTFE), and borosilicate glass. These materials leach contaminants at very low concentrations, which minimizes so-called container effects.¹⁸ The leak rates of all seals and connectors were checked with a leak detector (Varian 938-41, Varian Inc., Lexington, MA) to minimize the possibility of any external contaminants before any fluid was introduced into the loop. The sealed loop ($\sim 12\ell$ total vol-

ume) was filled with American Society for Testing and Materials (ASTM) type I water (environmental grade, Fisher Scientific, Waltham, MA) using a procedure similar to that of Herbert *et al.*⁷ The closed-loop system described here is effective at removing particulates and dissolved gases in the fluid by continuous circulation of the fluid through the filters and degassing chamber. The filtration system was modeled after a commercial system (Thermo Scientific Barnstead E-Pure, Thermo Scientific, Asheville, NC) for producing ASTM type I water. It was designed to keep the water purity to ASTM type I standards and uses five separate filters. The primary filter was a carbon-block membrane cartridge (pore size $0.15\text{ }\mu\text{m}$) used to remove bacteria before the fluid was allowed to pass through two de-ionization cartridges. The de-ionization cartridges were used to maintain the water resistivity at $16\text{ M}\Omega\text{ cm}$. A 100 nm PTFE membrane filter acted as a polishing filter. Finally, a commercially available ultrafilter (model name Biopak, Millipore Corporation, Billerica, MA) acted as a molecular sieve with a cutoff weight of 20 000 Da.

The filtration system was found to return the fluid to a minimal baseline particulate content by measuring the particulate content of manufacturer ultrapure water (straight from the bottle), water extracted from the loop after a typical data run, and water extracted from the loop after a typical filtering and degassing cycle (removal of gases from the fluid will be discussed in the next paragraph). These samples were sent to a commercial laboratory (Particle Measuring Systems, Boulder, CO) and the particulate content in the size range of $0.1\text{--}20\text{ }\mu\text{m}$ was measured via light scattering methods.

The cumulative volume fraction of particulates as a function of size is shown in Fig. 2. The relatively large volume fraction of particulates from the group B data indicated that some particulates were leached into the fluid after a data run. However, after the fluid was filtered and degassed, the

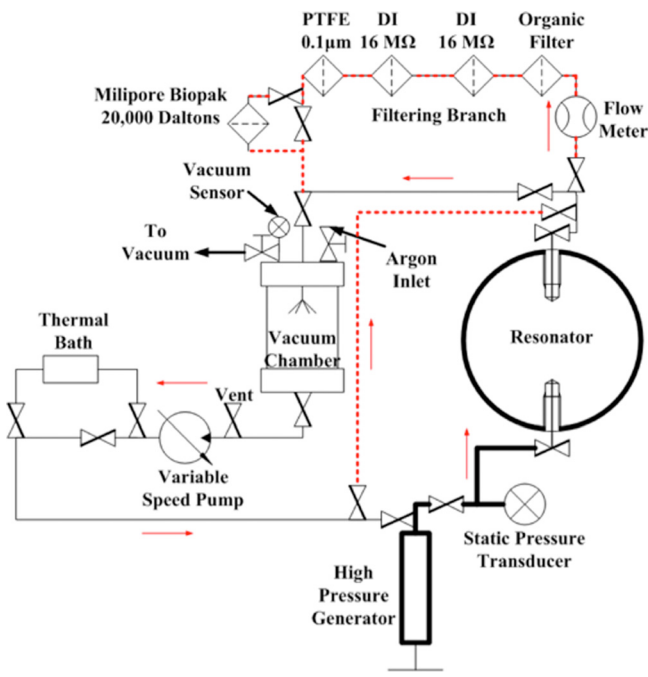


FIG. 1. (Color online) Diagram of fluid loop. The thin, solid lines are 303 stainless steel tubing for low pressure flow. The thick lines indicate the high pressure section of the loop. Dashed lines are PTFE tubing. The thin arrows indicate flow direction.

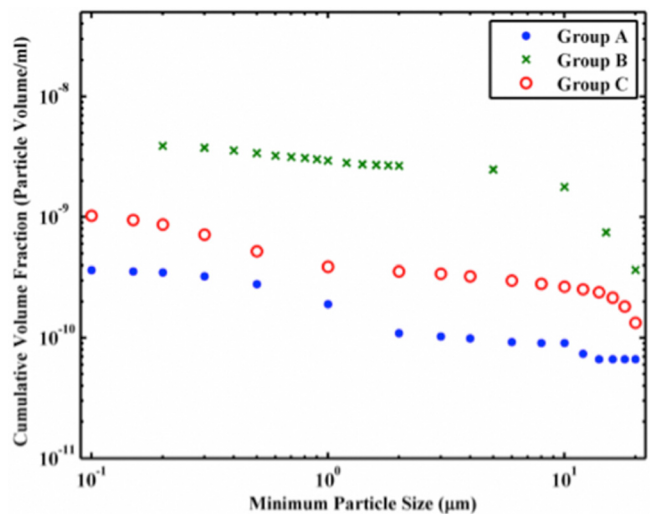


FIG. 2. (Color online) Measured cumulative volume fraction (up to $20\text{ }\mu\text{m}$) of particulates in the testing fluid (ultrapure water) as a function of minimum particulate size. Group A samples were water straight from the supply, group B samples were extracted from the loop after a typical data run, and group C samples were extracted from the loop after a typical filtering and degassing cycle.

number of particulates was reduced to near the baseline of the raw fluid as indicated by the relatively close values of groups A and C. This indicated that the filtration process was adequate to reduce the particulate content to an acceptable level.

Dissolved gases were removed from the fluid by evacuating the vacuum chamber with a positive displacement pump (model 15400, Robinair SPX Corporation, Owatonna, MN) while circulating the fluid through the chamber. The factor micron rating of the pump was $20 \mu\text{bars}$, and the free air displacement of the pump was specified to be $4 \text{ ft}^3/\text{min}$. A liquid nitrogen trap (placed in-line between the vacuum chamber and the vacuum pump) prevented both oil vapors drifting through the vacuum line into the closed loop and water vapor from damaging the pump. The chamber was typically backfilled to 400 Torr with argon to facilitate circulation of the fluid through the filtering branch of the loop.

The fluid temperature was adjusted via a cold plate immersed in a 24ℓ bath filled with a 50% solution of ethylene glycol to within 0.1°C by a constant temperature circulator (Polystat 12101-10, Cole-Parmer, Vernon Hills, IL). The temperature of the fluid within the sphere was observed to increase by several degrees over the course of a data run due to absorption of acoustic energy. Two equipment cooling fans (p/n 1976k43, McMaster-Carr, Atlanta, GA) were used to circulate the air around the resonator to minimize this heating.

A screw piston (model 50-6-15, High Pressure Equipment Company, Erie, PA) was used to generate overpressure in the high pressure section of the loop. The piston shaft was constructed from 17-4PH stainless steel. The static pressure in the high pressure section of the loop was measured with a flush-mounted pressure transducer (MP-40B, Micron Instruments, Simi Valley, CA), manufactured from highly corrosion resistant titanium (type 6AL4V).

3. Cavitation generation electronics

A block diagram of the driving electronics is seen in Fig. 3. The setup is modeled after Roy *et al.*⁸ The system was driven continuously at the (0,6) mode while increasing

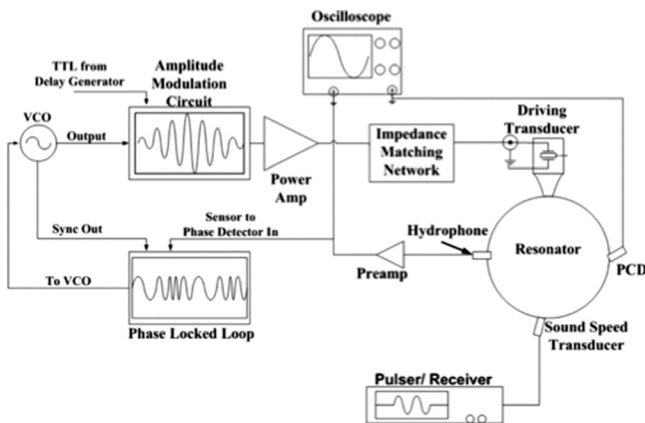


FIG. 3. Diagram of driving electronics for cavitation generation. The function generator is operated as a voltage controlled oscillator (VCO) so that the phase locked loop can maintain the driving frequency at resonance. Cavitation events are detected using a passive cavitation detector, or PCD.

the driving level with a custom-designed amplitude modulation (AM) circuit until inertial cavitation occurred. The resonator was excited with four custom-designed transducers connected electrically in parallel. The impedance presented by the drivers was quite large at the frequencies of interest ($\sim 1 \text{ k}\Omega$) and it was necessary to use adjustable transformers (turn ratio 1/9.64, CMI-4627 0938, Corona Magnetics, Inc., Corona, CA) in series with each driver to match the load to the power amplifier (1140LA, ENI Power Systems, Rochester, NY).

The fluid temperature would typically drift over the course of a measurement, resulting in shifts of the sound speed and therefore resonant frequency of the system. Since the quality factor of the system was so large, it was critical that the system be continuously driven at resonance.¹⁶ This was accomplished by the use of a custom-designed phase locked loop (PLL) manufactured by IDI.

The sound speed of the fluid was determined by measuring the relative echo time of consecutive reflections of an ultrasonic propagating across the resonator cavity. A 10 MHz contact transducer (M1054, Olympus NDT Inc., Waltham, MA) was excited with a pulser/receiver unit (5800, Olympus NDT Inc., Waltham, MA). The time-of-flight was determined by measuring the time difference between the envelope of the first and second set of reflections, and the sound speed computed assuming the path length was twice the nominal diameter of the fluid-filled resonator (20.32 cm, 8 in.). This procedure was automated using a MATLAB data-acquisition script (The Mathworks, Natick, MA). These sound speed measurements were used to calculate the approximate resonant frequency.

4. Passive cavitation detection

Inertial collapses were passively detected by measuring the high-amplitude shock waves emitted by the collapsing cavity via an ultrasonic delay line transducer affixed to the outer surface of the resonator ($f_C = 15 \text{ MHz}$, V205, Olympus NDT Inc., Waltham, MA). The transducer signal was high-pass filtered ($f_C = 1 \text{ MHz}$) and amplified (+10 dB) using a pulser/receiver unit (5072PR, Olympus NDT Inc., Waltham, MA), creating a passive cavitation detector (PCD) system. The PCD signal was used to trigger an oscilloscope (LT264, LeCroy Corporation, Chestnut Ridge, NY) recording the output of the aforementioned hydrophone. The PCD signal also triggered a digital delay generator (DG645, Stanford Research Systems, Inc., Sunnyvale, CA), which reset the AM circuit after a recovery period of 20 s.

B. Data collection procedure

The elements of the experimental setup outlined previously were combined in the following data collection procedure.

- (1) *Liquid preparation:* The fluid was circulated through the filtering branch for one circuit (approximate circulation time 45 min). The liquid was then degassed for 40 min by evacuating the vacuum chamber while continuously circulating the fluid at an approximate rate of 270 ml/min . At

the end of the degassing cycle, the measured dissolved oxygen concentration was $<0.2\text{ mg/ml}$ (approximately 2% of saturation). If necessary, the liquid was cycled further until the desired fluid temperature was reached.

- (2) *Driver preparation:* The high pressure section of the loop (see Fig. 1) was isolated, and the sphere was pressurized to the desired level using the high pressure generator. The approximate acoustic resonant frequency was determined by measuring the sound speed of the fluid and comparing the result to a previously determined empirical relation between sound speed and resonant frequency. The cores of the matching transformers were then adjusted such that the power factor was unity at resonance, resulting in an apparent load of $50\ \Omega$ to the amplifier and thus maximum electrical power transfer.
- (3) *Mode locking:* The waveform generator was then switched to frequency modulation mode (voltage controlled oscillator), and the PLL was used to keep the driving frequency locked at resonance. Typically, the hydrophone signal was pre-amplified and passed through a narrowband filter ($\sim 2\text{ kHz}$), and was used as the input signal to the phase detector on the PLL.
- (4) *Quiescent state/ramp rate:* The acoustic pressure was then adjusted to the quiescent amplitude, such that $P_{\text{cav}}/P_{\text{quiescent}} \sim 1.7$, where P_{cav} is the approximate cavitation threshold. This quiescent amplitude was chosen to accommodate the limited range of the voltage ramp on the AM circuit. After the quiescent amplitude was set, the ramp rate was adjusted so that the acoustic pressure increased by 1 bar/s. There was no statistically significant variation of the threshold with the ramp rate (over the range 0.5–27 bars/s) or quiescent amplitude ($P_{\text{cav}}/P_{\text{quiescent}} \sim 1.25\text{--}1.75$). However, the scatter in the data, and therefore the standard deviation, was proportional to the quiescent amplitude. This observation is in agreement with Roy *et al.*⁸
- (5) *Data collection:* The data collection was automated using a MATLAB script. The automation was carried out by a personal computer using GPIB (IEEE-488) protocol communications over a USB link. The GPIB control arrangement is shown in Fig. 4. The automated process began by disengaging the TTL pulse from the delay generator, discharging the AM circuit, and allowing the acous-

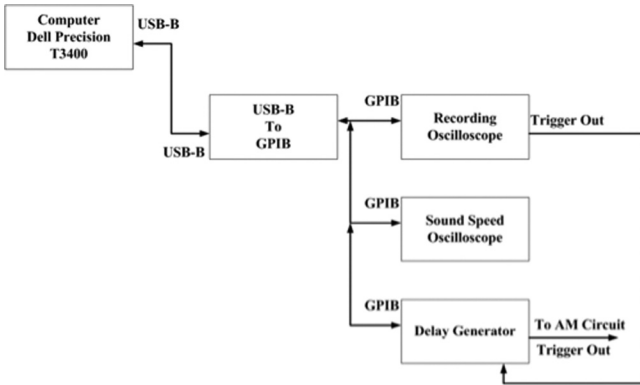


FIG. 4. Block diagram of computer control for automation of data collection procedure.

tic pressure to increase until the onset of inertial cavitation was detected via PCD. Once the PCD signal reached the predetermined threshold (typically 200 mV), the oscilloscope recording the hydrophone signal was triggered. The ramp was then disengaged by a TTL signal from the delay generator, and the system returned to its quiescent state for 20 s (the approximate recovery time of the system was 1 s). Typically, 100 cavitation events were recorded (one per ramping cycle).

- (6) *Post measurement:* When the automated measurement was finished, the fluid's sound speed, c_1 , was determined in order to estimate the pressure drift over the course of the measurement. Since the temperature may also vary over the course of the measurement, the sphere was set to a known pressure, and the sound speed, c_2 , was re-measured. Since the static pressure was known for c_2 the temperature of the fluid could be calculated using the well-known relationship between water's sound speed, pressure, and temperature.¹⁹ The temperature calculated from c_2 was then used with c_1 to calculate the pressure drift, assuming that the fluid temperature did not drift while adjusting the static pressure (adjustment time $\sim 1\text{ min}$).

III. RESULTS

The static pressure dependence of the threshold over the temperature range $18\text{ }^\circ\text{C}$ – $34\text{ }^\circ\text{C}$ is plotted in Fig. 5. Each data point is the mean of the measured threshold of the data set. The total number of recorded cavitation events per data set at each static pressure, typically 100, is recorded in Table I. The vertical error bars are the standard deviation in the threshold for the data set. The isothermal dependence of the threshold is approximately linear with the static pressure. Each isotherm threshold shown in Fig. 5 was fit to a linear curve. These best-fit linear parameters are shown in Table II.

The mean cavitation threshold over the range of measured temperatures is plotted as a function of the static

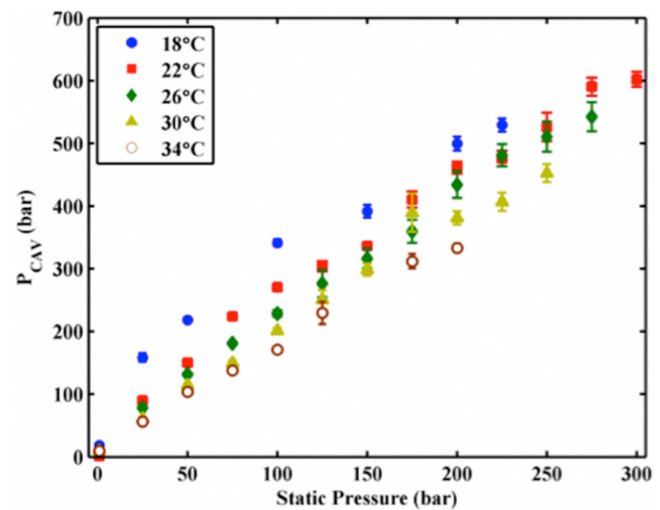


FIG. 5. (Color online) The static pressure dependence of the cavitation threshold plotted as a function of fluid temperature ($\pm 2\text{ }^\circ\text{C}$) over the range $18\text{ }^\circ\text{C}$ – $34\text{ }^\circ\text{C}$. The vertical error bars are the standard deviation of the threshold for the data set, and are not large enough to be seen below 100 bars.

TABLE I. Average number of measured threshold per data run at each static pressure.

P_{stat} (bar)	Average number of events per data run
1–225	100
250	75
275	75
300	20

pressure in Fig. 6. The linearity of the temperature-independent threshold data suggests that it can be used as a rule of thumb for calculating the static pressure dependence of the cavitation threshold,

$$P_{\text{cav}} = 1.92P_{\text{stat}} + 34.64, \quad (2)$$

where P_{cav} , the amplitude of the acoustic pressure at the cavitation threshold, and P_{stat} , the static pressure, are both in units of bar. The coefficient of determination and standard deviation of the mean for Eq. (2) are $r^2 = 0.997$ and $\sigma_{\bar{X}} = 11.12$ bar, respectively.

The temperature dependence of the cavitation threshold from 1 to 250 bars static pressure is plotted in Fig. 7. The data points and vertical error bars are the mean and standard deviation of the data set, and the horizontal error bars are the drift in temperature.

IV. DISCUSSION

A. Temperature dependence of threshold

When possible, the threshold at each static pressure was measured from room temperature (17°C – 22°C) up to 35°C . In practice, once the sound speed was greater than 1540 m/s it became difficult to produce repeatable data sets because the (0,6) mode overlapped with another nearby mode. This sound speed occurred at lower temperatures as the static pressure was increased, thus limiting the range of temperatures investigated for increasing static pressure.

There was a noticeable influence of temperature on the cavitation threshold at elevated static pressures. For example, the threshold varied by approximately 150 bars over a 15°C range at 100 bars static pressure. Previous measure-

TABLE II. Best-fit parameters for linear fit of P_{cav} (bar) as a function of P_{stat} (bar) over the range of measured temperatures. The goodness-of-fit parameters coefficient of determination (r^2) and the standard error ($\sigma_{\bar{X}}$) are in the last two columns.

Fluid temperature ($^\circ\text{C}$)	Slope (bar/bar)	Ordinate intercept (bar)	r^2	$\sigma_{\bar{X}}$ (bar)
18	2.44	96.82	0.999	0.981
20	1.94	70.89	0.968	39.837
22	1.96	48.75	0.985	24.976
24	1.75	77.84	0.965	24.246
26	1.99	24.82	0.996	10.696
28	1.68	35.73	0.998	6.519
30	1.87	15.54	0.985	20.158
32	1.87	5.95	0.995	9.451
34	1.64	13.23	0.996	9.280

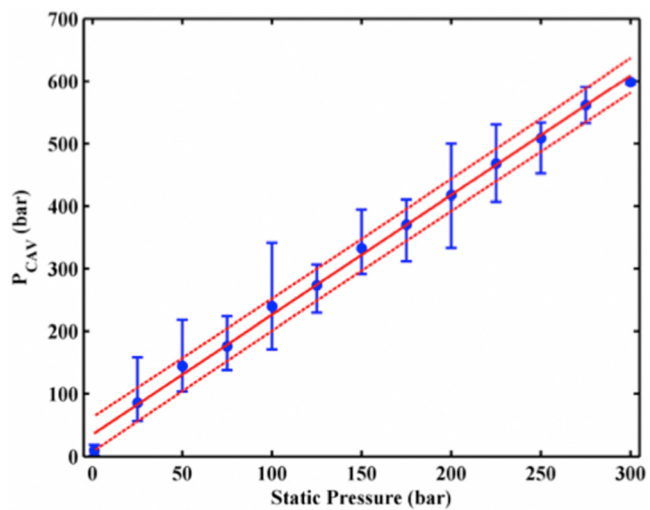


FIG. 6. (Color online) The static pressure dependence of the cavitation threshold. Each data point represents the mean threshold at all temperatures. The vertical bars are the spread in P_{cav} over the measured temperature range. The solid line is a linear fit to the data [Eq. (2)], and the dashed lines are the 95% confidence intervals of the fit to the data.

ments found that the temperature dependence of the threshold was strong for fluids with large amounts of dissolved gases,⁵ whereas the data in Fig. 7 are for well-degassed (~ 2 kPa partial pressure) water, and yet still strongly dependent on temperature. However, the vapor pressure and surface tension of water depend exponentially on temperature, which, in turn, influence the nucleating mechanisms of the cavitation.

To investigate the nucleation mechanism in these experiments, the temperature-dependent threshold was compared to the crevice model for nucleation.^{14,20} The model assumes gas pockets are stabilized in the conical crevices of pre-existing dirt particles present in the fluid, and has correlated well with experimental measurements when the geometry of the crevice is well known.²¹ There is some validation

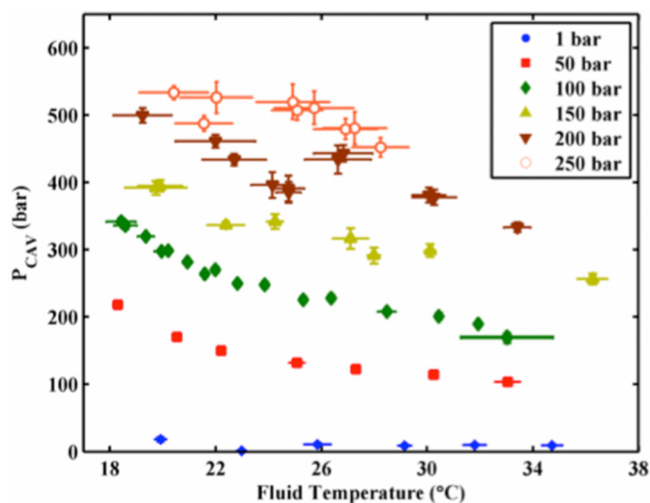


FIG. 7. (Color online) The temperature dependence of the cavitation threshold over the range 1–250 bars static pressure. The markers are the mean measured threshold for the data run. The vertical error bars represent the standard deviation of the measured threshold, while the horizontal bars are the drift in temperature over the data run.

of this model as being the most likely source of nucleation as the previously mentioned analysis of the particulate content of the liquid indicated that there were some 10^6 particles/ m^3 present for particle sizes in the range of $0.1\text{--}20\ \mu\text{m}$. Any of these particulates may contain one or more potential crevice nucleation sites. Furthermore, previous measurements have shown that the crevice model is the most likely candidate for bubble nucleation.¹⁷ Nucleation from cavitation at the walls is usually neglected in resonant systems, as the modes are chosen such that the acoustic pressure is small compared to the pressure anti-node in the bulk of the fluid.⁶ In addition, there are several pressure nodes and anti-nodes along the radial pressure profile that would trap any bubble before it reached the center. Nucleation from cosmic rays also seems unlikely to contribute significantly to a given data set, as only about 3 neutrons/h with energy $>10\ \text{MeV}$ (those with sufficient energy to induce nucleation⁶) are estimated to reach central pressure anti-node.

Crum⁵ was able to write the crevice model in terms of experimentally measured quantities of typical crevice geometries (conical crevice) and incorporate the effects of surface tension,

$$P_{\text{crevice}} = P_H - P_V - \gamma P_G + \frac{P_H - P_V - P_G}{\delta} \left[\cos(\phi) \left(\frac{C}{\sigma} - 1 \right) + \sin(\phi) \left[1 - \left(\frac{C}{\sigma} - 1 \right)^2 \right]^{1/2} \right], \quad (3)$$

where P_H is the hydrostatic pressure of the liquid, P_V is the vapor pressure, P_G is the partial pressure of gas, σ is the water/gas surface tension, C is a parameter that depends on the surface properties of the solid, γ measures the ability of a nucleating gas pocket to maintain equilibrium gas pressure, and δ and ϕ are parameters that depend on the geometry of the crevice.

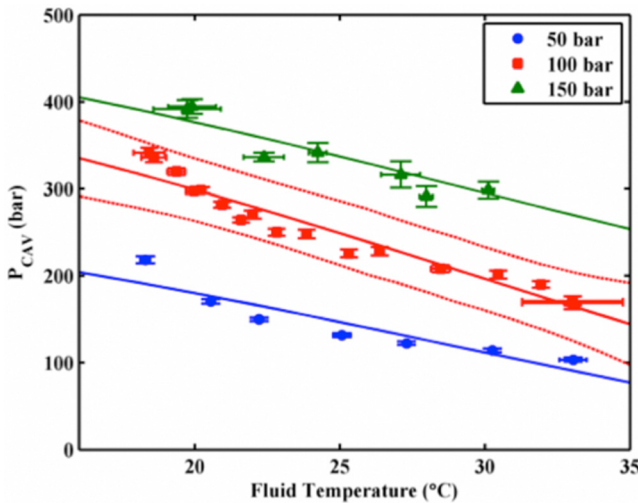


FIG. 8. (Color online) P_{cav} as a function of fluid temperature at static pressures of 50, 100, and 150 bars. The solid lines are fits to Crum's model for nucleation from a crevice [Eq. (3)]. The dashed lines are the 95% confidence intervals of the fit to the data at 100 bars.

TABLE III. Best-fit parameters of crevice model to temperature-dependent threshold. The 95% confidence intervals are shown in parentheses. The goodness-of-fit parameters coefficient of determination (r^2) and the standard error ($\sigma_{\bar{X}}$) are in the last two columns.

P_{stat} (bar)	δ (no unit)	ϕ (deg)	r^2	$\sigma_{\bar{X}}$ (bar)
50	$0.00512 (\pm 0.0025)$	$212.91 (\pm 0.28)$	0.847	16.81
100	$0.00681 (\pm 0.001)$	$212.91 (\pm 0.06)$	0.934	14.58
150	$0.0129 (\pm 0.0042)$	$212.57 (\pm 0.28)$	0.906	16.0

The temperature dependence of the cavitation threshold at 50, 100, and 150 bars static pressure is plotted in Fig. 8 along with a temperature-dependent fit (via the temperature dependence of vapor pressure and surface tension) of Eq. (3) to the data using a non-linear least-squares routine. δ and ϕ were used as fitting parameters, and γ was set to 1. P_G was set equal to the temperature-dependent vapor pressure, and C was set to 0.05 N/m. Representative values for the fitting parameters at 50, 100, and 150 bars static pressure are shown in Table III.

The data fall within the 95% confidence intervals of the fit in each case, which is suggestive that the model is consistent with the temperature dependence of the data. The spread of the confidence intervals likely does not necessarily reflect that Eq. (3) is a bad fit to the data, but that there is a variety of crevice geometries present in the liquid. It is likely that the actual nucleating particulate, and therefore the crevice geometry (possibly not a conical crevice), varied from measurement to measurement and that the best-fit parameters represent the mean values of the crevice geometry.

Besides the crevice model, the temperature dependence of the data was also modeled by an exponential decay of the form $P_{\text{cav}} = A \exp[-\Gamma T]$ up to 250 bars. The best-fit decay constant (using a non-linear least-squares method) Γ is plotted as a function of the static pressure in Fig. 9. The decay constant itself decays exponentially with the static pressure and has the following form:

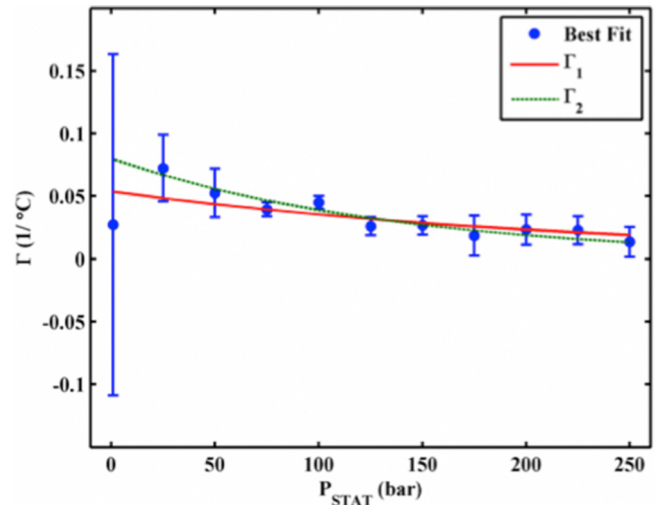


FIG. 9. (Color online) Exponential coefficient τ as a function of static pressure. The vertical error bars come from the 95% confidence intervals of the fit to the data. The solid line is the exponential fit of τ to the entire static pressure range [Eq. (4)]. The dashed line is the exponential fit of τ to 25–250 bars [Eq. (5)].

$$\Gamma = 0.0536 \exp [-0.004178 P_{\text{stat}}]. \quad (4)$$

The threshold at 1 bar deviates from the linear predictions of the threshold dependence of static pressure (see the discussion on the static pressure dependence of the threshold). If the data point at 1 bar is neglected, the amplitude and decay constants in Eq. (4) become

$$\Gamma = 0.0799 \exp [-0.007245 P_{\text{stat}}]. \quad (5)$$

The coefficient of determination is $r^2 = 0.484$ and the standard error is $\sigma_{\bar{x}} = 1.32 \times 10^{-2}$ for Eq. (4). For Eq. (5), the coefficient of determination is $r^2 = 0.914$ and the standard deviation of the mean is $\sigma_{\bar{x}} = 5.60 \times 10^{-3}$.

The form of Eqs. (4) and (5) suggests that the influence of temperature on the threshold diminishes as the static pressure of the fluid is increased. If the upper range of strong temperature dependence is taken to be the decay constants of Eqs. (4) and (5), the cavitation threshold should be largely independent of the fluid temperature in the range of 138–240 bars. Hence, beyond this range of static pressures, the temperature dependence of vapor pressure and surface tension no longer have as strong an influence on the crevice model, and nucleation may depend solely on overcoming the large overpressure.

B. Static pressure dependence of the threshold

The cavitation threshold increases linearly with the static pressure as evident in Figs. 5 and 6, especially above 1 bar. The deviation from linearity at 1 bar was also observed by Herbert *et al.*,⁷ who concluded it was due to either the presence of impurities in the form of air bubbles or that the properties of the focused transducer were pressure dependent. For the current results, the consistency of the data with the crevice model suggests that any trapped gas pockets are more easily liberated from the crevice at low static pressures. This would be the case if the contact angle were initially at the so-called receding contact angle¹⁴ and the contact line were near the mouth of the crevice. However, beyond 1 bar static pressure the contact angle would increase to the so-called advancing angle, which would increase the threshold and thus account for the deviation from linear behavior below 1 bar. As the static pressure increased, the contact angle would remain fixed at the advancing contact angle, and the contact line would regress toward the apex of the crevice. The regression of the contact line into the crevice would correspond to the linear portion of the threshold dependence on static pressure. Thus in principle it should be possible to analyze the threshold data obtained in this work in conjunction with Eq. (3) and others from Apfel¹⁴ to determine something of the nature of the nucleating particles present in the liquid.

Unfortunately, it is not possible to find a unique solution to Eq. (3) without making some additional assumptions. To understand why, consider Eq. (3) more closely. Notice that the term in square brackets on the right-hand side is the sum of two orthogonal trigonometric functions. Although the sine and cosine terms are multiplied by different coefficients,

their sum must be such that it produces a constant value providing a best fit to any set of the threshold data. That there will be an infinite number of such sets is made obvious by rewriting Eq. (3) as (see the Appendix)

$$P_{\text{crevice}} = P_H - P_V - \gamma P_G + \frac{P_H - P_V - P_G}{\delta} \sin(\phi + \theta). \quad (6)$$

The term in square brackets in the original equation is now seen to be a simple sine function of ϕ plus a phase angle θ . Because θ is a function of C and σ , changing either or both of their values has no effect on the shape of the curve; only the position of the curve is changed. For the values of C and σ assumed here, 50 and 72 mN/m, respectively, $\theta = -0.3105$.

One potential way forward is to equate the measured cavitation threshold, P_{cav} , with the theoretical Blake threshold, P_{Blake} , for inertial cavitation. This approach allows calculation of the critical radius, R_c , which is the smallest bubble that will cavitate when exposed to P_{Blake} . If it is further assumed that $P_{\text{cav}} = P_{\text{Blake}}$, which is implicit in the application of Eq. (3) to the threshold data, and also that R_c is the radius of the opening of the crevice, a_c , then δ can be calculated using the following equation given by Apfel:¹⁴

$$a_c = \frac{2\sigma\delta}{P_H - P_V - P_G}. \quad (7)$$

The method was applied to the data for P_{cav} at 20 °C over the range of P_{stat} , 1–300 bars. As a first step, the values of the critical radii were calculated. These lie in the range $55.51 \leq R_c \leq 3.21$ nm. Consideration of the data for R_c suggests two different conclusions. As the static pressure increases, either smaller and smaller crevices nucleate smaller and smaller bubbles, or the gas pockets that nucleate at $P_{\text{stat}} = 1$ bar are pushed farther down into the crevices. Of course both cases may be true, and while there does not appear to be any simple method for distinguishing between them, this does not matter in terms of either the threshold for, or the energy concentrated in, the subsequent cavitation event. However, since the goal is to pursue information on the nature of the particles hosting the gas-containing crevices, and because the crevice model incorporates the second of these two possibilities, the latter was investigated further.

For the next step, the values of δ corresponding to the various R_c determined previously were calculated using Eq. (7). Then a representative data set was constructed by selecting the mean and standard deviation of the one threshold set at each value of P_{stat} obtained over a temperature range closest to 20 °C. For each value of δ , Eq. (3) was fit to the representative data set to determine the corresponding value of ϕ ; the smaller of the two possible values was selected in each case because the larger often produced non-physical results in subsequent analyses. A summary of the results obtained in this way is given in Table IV.

Next it was noted that the $\phi + \arccos(\delta) = 2\alpha_A - \alpha_R$ and $\phi - \arccos(\delta) = 2\beta - \alpha_R$. The model also requires that $\beta > 0$ and $\alpha_A \geq \pi/2 + \beta$. By assuming that $\beta = 0$, then the minimum possible values for α_A and α_R at each P_{stat} were calculated

TABLE IV. Results obtained with threshold data at 20°C assuming $P_{\text{cav}} = P_{\text{Blake}}$.

P_{stat} (bar)	P_{cav} (bar)	R_c (nm)	δ (no unit)	ϕ (rad)
1.0	18.10	55.510	0.0371	0.37015
25.0	116.23	10.416	0.1823	0.60768
50.0	170.40	7.893	0.2765	0.77096
75.0	223.53	6.398	0.3364	0.88133
100.0	297.49	4.812	0.3374	0.88324
125.0	329.67	4.644	0.4070	1.02299
150.0	394.61	3.885	0.4087	1.02661
175.0	410.33	4.039	0.4956	1.23120
200.0	499.81	3.170	0.4446	1.10586
225.0	530.45	3.112	0.4909	1.21883
250.0	533.35	3.354	0.5880	1.54635
275.0	590.72	3.010	0.5805	1.51145
300.0	595.84	3.213	0.6759	1.82625

from the values of δ and ϕ determined by the best fit to the experimental data. The average minimum values (\pm standard deviation) over the range of P_{stat} were $\alpha_A = 114.3^\circ \pm 11.0^\circ$ and $\alpha_R = 52.6^\circ \pm 12.1^\circ$. The maximum values of α_R and β were found from the fit to the experimental results for P_{cav} by assuming $\alpha_A = \alpha_R$. In some cases, this resulted in a value for $\alpha_A > 180^\circ$. Since the model does not permit this possibility, α_A was assigned to its maximum possible value (180°) when this occurred. The average maximum values over the range of P_{stat} were $\alpha_A = 165.0^\circ \pm 21.0^\circ$, $\alpha_R = 154.0^\circ \pm 20.6^\circ$, and $\beta = 50.7^\circ \pm 11.8^\circ$. In this way, the following limitations were placed on the geometry of the nucleating crevices: $114.3^\circ \leq \alpha_A \leq 165.0^\circ$, $52.6^\circ \leq \alpha_R \leq 154.0^\circ$, and $0.0^\circ < \beta \leq 50.7^\circ$.

The foregoing results included only a small fraction of the total data available. To rectify this difficulty, the analysis was repeated on the five groups of data used to produce Fig. 5, but without the averaging of similar data sets used in Fig. 5. That is, at each value of P_{stat} , each of the 105 data sets was assigned to one of five groups based on the average temperature of the liquid during that experimental run: $18^\circ \pm 2^\circ$, $22^\circ \pm 2^\circ$, $26^\circ \pm 2^\circ$, $30^\circ \pm 2^\circ$, or $34^\circ \pm 2^\circ$. Each temperature group was then analyzed as described previously. A summary of the ranges for each angle is given in Table V; the results at 20°C are shown for comparison. The consistency of the results tends to support the method of data analysis.

TABLE V. Results for ranges of angles satisfying the crevice model for all pressures.

Temperature (°C)	α_A (deg)	α_R (deg)	β (deg)
20.0	114.29–164.99	52.57–153.99	0.00–50.71
18 ± 2	107.08–155.72	52.22–149.49	0.00–48.64
22 ± 2	119.80–171.59	52.84–156.43	0.00–51.79
26 ± 2	121.15–170.61	61.25–160.17	0.00–49.46
30 ± 2	128.42–171.37	71.79–157.68	0.00–42.95
34 ± 2	137.92–169.24	83.18–145.81	0.00–31.32

Unfortunately, the ranges of the angles in Table V are such that almost any material may conform to them. However, the results at the lower static pressures are less variable, with the data at $P_{\text{stat}} = 1$ bar being particularly useful. These are given in Table VI. The ranges for α_A encompass known values for some common polymers, including polypropylene²² and butyl rubber.²³ Of particular relevance to this work are values for PTFE also known as Teflon, because some of the components of the experimental apparatus comprised that polymer. Yasuda *et al.*²⁴ give the value for α_A as 100° . Substituting this into the above-mentioned equations for the analysis conducted on the data at 20°C yields the following: $\alpha_R = 86.7^\circ$ and $\beta = 7.9^\circ$. The advancing and receding contact angles for PTFE are provided by, Brewis and Mathieson²⁵ $\alpha_A = 106^\circ$ and $\alpha_R = 90^\circ$. Both of these values are within the ranges determined previously. The corresponding value for β depends on which value of these two parameters is chosen, but the range between the two is not great: $9.5^\circ \leq \beta \leq 13.9^\circ$.

Based on these results, it may be concluded that the particulates responsible for bubble nucleation in these experiments are some kind of polymer, and that the crevices from which the bubbles nucleate are relatively narrow. Further, if particles of PTFE are responsible for bubble nucleation in the present study, this may also help explain some of the variability in the results. PTFE is the most compressible of all common polymers. As the static pressure is increased, the particles will compress, and because the pressure within the gas trapped in a crevice does not change, the crevice angle, β , will decrease. Variation of β within a data set is not included in any of the modeling or analyses performed in this work.

As previously discussed, the crevice size is presumably decreasing with the static pressure because the contact angle is fixed at the so-called advancing contact angle and the contact line is forced further into the crevice when pressure is applied. Apfel¹⁴ suggests that a is approximately 1/5 of the effective crevice radius. If this were the case, the mote size at 1 bar would be roughly 55 nm, while at 25–250 bars the mean mote size would be ~ 1 nm. If the mote is assumed to be harbored in a particle an order of magnitude larger than the effective mote size, then the nucleating particulates would be roughly 300 nm at 1 bar and 5 nm for the particulates at 25–250 bars. The data collected for Fig. 2 indicate nearly 1×10^6 particulates/ml in the 100 nm size range,

TABLE VI. Results for ranges of angles satisfying the crevice model, $P_{\text{stat}} = 1$ bar.

Temperature (°C)	α_A (deg)	α_R (deg)	β (deg)
20.0	92.13–113.34	70.92–113.34	0.00–21.21
18 ± 2	92.14–114.61	69.67–114.61	0.00–22.47
22 ± 2	— ^a	—	—
26 ± 2	93.67–116.04	71.30–116.04	0.00–22.37
30 ± 2	94.23–115.85	72.61–115.85	0.00–21.62
34 ± 2	94.11–114.53	73.69–114.53	0.00–20.42

^aNo data were obtained in this temperature range.

which would indicate plenty of particulates in the size range required for nucleation at 1 bar static pressure. Since the number of particles per m^3 is inversely proportional to the particle size on a log–log scale, it could also be assumed that particulates much smaller than the smallest measured size (100 nm) would be in abundance in the fluid.

The absolute tension required to produce cavitation, $|P_{\text{cav}} - P_{\text{stat}}|$, for the average threshold is readily calculated from Eq. (2),

$$|P_{\text{cav}} - P_{\text{stat}}| = 0.92P_{\text{stat}} + 34.64. \quad (8)$$

The linear relation between the static pressure and the tension required to reach the cavitation threshold is in contradiction with the findings of Greenspan and Tscheigg⁶ and Strasberg.⁹ Herbert *et al.*⁷ also found the absolute tension required for cavitation in water to be essentially constant (although temperature dependent) up to 80 bars. To the authors' knowledge, the tensions reported by Herbert *et al.*⁷ (160–250 bars over the temperature range 2 °C–82 °C) were the largest values measured in water using an acoustic method. The largest measured tensions in water are generally accepted^{26–29} to be those of Briggs,³⁰ who could maintain up to 277 bar tension using a centrifugal method. Equation (8) indicates that the current data set requires 230 and 266 bars static pressure to reach the tensions measured by Herbert *et al.*⁷ and Briggs,³⁰ respectively. At 300 bars static pressure, the tension required for inertial cavitation is 310 bars, some 30 bars larger than Briggs' measurement. To the authors' knowledge, these results are the largest ever measured tension in water.

While these large tensions are impressive, there is still the discrepancy between the linear relationship between tension and static pressure for the current data set and the static pressure independent data of Briggs³⁰ and Herbert *et al.*⁷. Furthermore, the large static pressures required to reach the tensions required by Briggs³⁰ and Herbert *et al.*⁷ determined using Eq. (8) are somewhat surprising considering the quality of the fluid for the current results. The discrepancy may be accounted for from the varying experimental conditions. The methods for creating tension vary between using an acoustic source, as with the current data set and Herbert *et al.*,⁷ and that of Briggs' centrifugal method.³⁰ There is even variation among the acoustic methods, as Herbert *et al.*⁷ used a 1–2 cycle burst of a focused 1 MHz transducer to generate tension. Such high frequencies are well known to increase the cavitation threshold.³¹ In addition, the fluid temperature for both Briggs³⁰ and Herbert *et al.*⁷ were much lower than the current data set [2 °C, 10 °C, and the 26 °C average for Eq. (10), respectively]. The current data set shows that temperature can play a critical role in the threshold. For instance, at 18 °C, the lowest temperature employed in the experiments reported here, Table II indicates that the static pressure required to reach the tensions reported by Herbert *et al.*⁷ and Briggs³⁰ would be reduced to 106 and 125 bars, respectively. A reduction of fluid temperature in the current experiment to levels comparable to those of Herbert *et al.*⁷ and Briggs³⁰ would likely increase the measured threshold and thereby reduce the discrepancy between the data sets.

V. SUMMARY AND CONCLUSIONS

The cavitation threshold ultimately limits the amount of energy that can be stored within the resonant system. Hence, the onset of cavitation must be suppressed to maximize the energy stored within a resonant system. In this study, cavitation was suppressed by increasing the static pressure of the fluid. The inertial cavitation threshold was found to be linearly dependent on the static pressure and also temperature dependent. The linear dependence of the tension required for inertial cavitation on static pressure was inconsistent with previous measurements, although the tension was larger than those studies.

The tensional strength of the liquid was likely limited by its impurities,¹⁷ and the homogeneous nucleation threshold (HNT)³² was never reached. However, the HNT is only weakly dependent on the static pressure, with a slope of ~ 1 [bar/bar].¹⁷ If the linear fit of Eq. (2) is applicable at static pressures beyond 300 bars, the crevice-dominated threshold and HNT should intersect at ~ 2.14 kbars static pressure. Therefore, beyond 2.14 kbars the threshold would no longer be dictated by the particulate content (i.e., the nucleation sites would all be crushed) but by homogeneous nucleation and the spontaneous creation of vapor bubbles. It is unknown what, if any, role temperature would have at such a large static pressure. These results indicated that the role of temperature was quite large, although it had a diminishing effect past ~ 200 bars static pressure, well within the region of crevice nucleation.

ACKNOWLEDGMENTS

The authors thank the technical staff at Impulse Devices, Inc., in particular Yuri Pishchalnikov, Joe Wellhoff, Brant Callahan, and Henry Tardif, as well as the technical staff at the National Center for Physical Acoustics, in particular Paul Dakin, Ronnie Oswalt, and Gary Daugherty, for their expertise and assistance with the construction of various aspects of the experimental setup. This work was funded by Impulse Devices, Inc.

APPENDIX: SIMPLIFYING THE EQUATION FOR NUCLEATION

The original form of the equation for the threshold for bubble nucleation from a crevice is

$$\begin{aligned} P_{\text{crevice}} &= P_H - P_V - \gamma P_G \\ &+ \frac{P_H - P_V - P_G}{\delta} \left[\cos(\phi) \left(\frac{C}{\sigma} - 1 \right) \right. \\ &\left. + \sin(\phi) \left[1 - \left(\frac{C}{\sigma} - 1 \right)^2 \right]^{1/2} \right]. \end{aligned}$$

Let

$$A = \left(\frac{C}{\sigma} - 1 \right), \quad B = \left[1 - \left(\frac{C}{\sigma} - 1 \right)^2 \right]^{1/2} = [1 - A^2]^{1/2}.$$

Then,

$$P_{\text{crevice}} = P_H - P_V - \gamma P_G + \frac{P_H - P_V - P_G}{\delta} [A \cos(\phi) + B \sin(\phi)],$$

$$P_{\text{crevice}} = P_H - P_V - \gamma P_G + \frac{P_H - P_V - P_G}{\delta} A \left[\cos(\phi) + \frac{B}{A} \sin(\phi) \right].$$

Let

$$\cot(\theta) = \frac{B}{A}, \quad \theta = \arccot \left[\left(\frac{1 - A^2}{A^2} \right)^{1/2} \right].$$

Note, θ is not necessarily the principal value.

Then,

$$\begin{aligned} \left[\cos(\phi) + \frac{B}{A} \sin(\phi) \right] &= \cos(\phi) + \cot(\theta) \sin(\phi) \\ &= \frac{\sin(\theta) \cos(\phi) + \cos(\theta) \sin(\phi)}{\sin(\theta)} \\ &= \frac{1}{\sin(\theta)} \sin(\phi + \theta) \\ &= \left[1 + \left(\frac{B}{A} \right)^2 \right]^{1/2} \sin(\phi + \theta) \\ &= \frac{1}{A} \sin(\phi + \theta). \end{aligned}$$

Finally,

$$P_{\text{crevice}} = P_H - P_V - \gamma P_G + \frac{P_H - P_V - P_G}{\delta} [\sin(\phi + \theta)].$$

- ¹H. Frenzel and H. Schultes, "Luminescenz im ultraschallbeschickten wasser (Luminescence in the ultrasound-fed water)," *Z. Phys. Chem. Abt. B* **27**, 421–424 (1934).
- ²H. G. Flynn, "Method of generating energy by acoustically induced cavitation fusion and reactor therefor," U.S. patent 4,333,796 (June 8, 1982).
- ³D. F. Gaitan, R. A. Tessien, R. A. Hiller, J. Gutierrez, C. Scott, T. J. Matula, L. A. Crum, R. G. Holt, C. C. Church, and J. L. Raymond, "Transient cavitation in high-quality-factor resonators at high static pressures," *J. Acoust. Soc. Am.* **127**, 3456–3465 (2010).
- ⁴D. F. Gaitan, L. A. Crum, C. C. Church, and R. A. Roy, "Sonoluminescence and bubble dynamics for a single, stable, cavitation bubble," *J. Acoust. Soc. Am.* **91**, 3166–3183 (1992).
- ⁵L. A. Crum, "Tensile strength of water," *Nature (London)* **278**, 148–149 (1979).
- ⁶M. Greenspan and C. E. Tscheigg, "Radiation-induced acoustic cavitation," *J. Res. Natl. Bur. Stand., Sec. C* **71**, 299–312 (1967).

- ⁷E. Herbert, S. Balibar, and F. Caupin, "Cavitation pressure in water," *Phys. Rev. E* **74**, 041603 (2006).
- ⁸R. A. Roy, A. A. Atchley, L. A. Crum, J. B. Fowlkes, and J. J. Reidy, "A precise technique for the measurement of acoustic cavitation thresholds and some preliminary results," *J. Acoust. Soc. Am.* **78**, 1799–1805 (1985).
- ⁹M. Strasberg, "Onset of ultrasonic cavitation in tap water," *J. Acoust. Soc. Am.* **31**, 163–176 (1959).
- ¹⁰F. G. Blake, Jr., "The tensile strength of liquids, a review of the literature," Tech. Memo No. 9, Acoustics Research Laboratory, Harvard University (1949).
- ¹¹K. Davitt, A. Arvengas, and F. Caupin, "Water at the cavitation limit: Density of the metastable liquid and size of the critical bubble," *Europhys. Lett.* **90**, 16002 (2010).
- ¹²N. E. Harvey, D. K. Barnes, W. D. McElroy, A. H. Whiteley, D. C. Pease, and K. W. Cooper, "Bubble formation in animals," *J. Cell. Comp. Physiol.* **24**, 1–22 (1944).
- ¹³A. Evans, "The influence of modest overpressure on the persistence of air bubbles in water," in *Cavitation and Inhomogeneities in Underwater Acoustics*, edited by W. Lauterborn (Springer, Gottingen, 1979), pp. 90–94.
- ¹⁴R. E. Apfel, "The role of impurities in cavitation-threshold determination," *J. Acoust. Soc. Am.* **48**, 1179–1186 (1970).
- ¹⁵M. R. Moldover, J. B. Mehl, and M. Greenspan, "Gas-filled spherical resonators," *J. Acoust. Soc. Am.* **79**, 253–272 (1986).
- ¹⁶J. L. Raymond, K. B. Bader, J. Mobley, D. F. Gaitan, R. A. Hiller, and R. A. Tessien, "Characterization of a large volume spherical resonator for studies of acoustically induced cavitation in liquids," *J. Acoust. Soc. Am.* **122**, 2991 (2007).
- ¹⁷K. B. Bader, "Inertial cavitation threshold dependence on static pressures," Ph.D. thesis, University of Mississippi, Oxford, MS, 2011.
- ¹⁸A. D. Bangham and M. W. Hill, "Distillation and storage of water," *Nature (London)* **237**, 408 (1972).
- ¹⁹C. Chen and F. J. Milero, "Reevaluation of Wilson's sound-speed measurements for pure water," *J. Acoust. Soc. Am.* **60**, 1270–1273 (1976).
- ²⁰A. A. Atchley and A. Prosperetti, "The crevice model of bubble nucleation," *J. Acoust. Soc. Am.* **86**, 1065–1084 (1989).
- ²¹B. M. Borkent, S. Gekle, A. Prosperetti, and D. Lohse, "Nucleation threshold and deactivation mechanisms of nanoscopic cavitation nuclei," *Phys. Fluids* **21**, 102003 (2009).
- ²²M. Kogoma, H. Kasai, K. Takahashi, T. Moriwaki, and S. Okazaki, "Wettability control of plastic surface by Cf₄-O₂ plasma and its etching effect," *J. Phys. D: Appl. Phys.* **20**, 147 (1987).
- ²³C. J. Budziak, E. I. Varga-Butler, and A. W. Neumann, "Temperature dependence of contact angles on elastomers," *J. Appl. Polym. Sci.* **42**, 1959–1964 (1991).
- ²⁴T. Yasuda, T. Okuno, and H. Yasuda, "Contact angle of water on polymer surfaces," *Langmuir* **10**, 2435–2439 (1994).
- ²⁵D. M. Brewis and I. Mathieson, "Pretreatments of fluoropolymers. A review of studies between 1990 and 1995," in *First International Congress on Adhesion Science and Technology*, edited by W. J. van Ooij and H. R. Anderson, Jr. (VSP, Utrecht, The Netherlands, 1998), pp. 267–284.
- ²⁶K. A. Mørch, "Reflections on cavitation nuclei in water," *Phys. Fluids* **19**, 072104 (2007).
- ²⁷R. D. Finch, "Influence of radiation on the cavitation threshold of degassed water," *J. Acoust. Soc. Am.* **36**, 2287–2292 (1964).
- ²⁸R. E. Apfel, "Acoustic cavitation inception," *Ultrasonics* **22**, 167–173 (1984).
- ²⁹T. G. Leighton, *The Acoustic Bubble* (Academic, San Diego, 1994).
- ³⁰L. Briggs, "Limiting negative pressure of water," *J. Appl. Phys.* **21**, 721–722 (1950).
- ³¹J. E. Barger, "Thresholds of acoustic cavitation in water," Tech. Memo No. 57, Engineering and Applied Physics, Harvard University, Office of Naval Research (1964).
- ³²C. C. Church, "Spontaneous homogeneous nucleation, inertial cavitation and the safety of diagnostic ultrasound," *Ultrasound Med. Biol.* **28**, 1349–1364 (2002).